Understanding the Structure-Activity Relationship of Additives for Durable Zn Metal Battery: A Case Study of Aromatic Molecules

Da-Qian Cai, [a] Haiyang Cheng, [b] Jin-Lin Yang, [a] Huan Liu, [a] Tao Xiao, [a] Xin Liu, [b], Minghua Chen, [b],and Hong Jin Fan*[a]

a D.-Q. Cai, J.-L. Yang, H. Liu, T. Xiao, Prof. Dr. H. J. Fan
School of Physical and Mathematical Sciences,
Nanyang Technological University
Singapore 637371
E-mail: fanhj@ntu.edu.sg

b H. Cheng, Prof. Dr. X. Liu, Prof. Dr. M. Chen
Key Laboratory of Engineering Dielectric and Applications (Ministry of Education), School of Electrical and Electronic Engineering
Harbin University of Science and Technology
Harbin 150080, China

Experimental Method

1. Electrolyte preparation

The bare 2 M $ZnSO_4$ electrolyte (ZSO) was prepared using $ZnSO_4 \cdot 7H_2O$ (AR) and deionized water. Stoichiometric amounts of Pyrazine, Pyrimidine, and Pyridazine (1.74 mM, 3.47 mM, and 6.94 mM) were dissolved into the as-prepared 2 M $ZnSO_4$ electrolyte.

2. Selection of optimized electrolytes

According to the classical nucleation theory and experiments, higher η_n is conducive to smaller radii of nucleation and more uniform deposition[1, 2]. Meanwhile, the growth overpotential η_g refers to the driving force required (1) mass transfer, de-solvation, charge transfer, and electro-crystallization process. The smaller η_g could ideally decrease the voltage drop caused by these processes. Therefore, it is reasonable to use the potential difference (ΔE) between η_n and η_g as a descriptor for electrolyte optimization. As shown in Figure S39, when the concentration of aromatic Pyrazine, Pyrimidine, and Pyridazine is 3.47 mM, the galvanostatic discharge curves exhibit the largest ΔE.

The optimized concentration is 3.47 mM, and the electrolytes were denoted as Pyr, Pym, and Pyd accordingly. Considering the higher specific area in thick NVO cathodes than the flat Cu and Zn foils and the adsorption of molecules at cathode surface, the concentration of Pyr, Pym, and Pyd was increased to 6.94 mM.

3. Synthesis of $NaV_3O_8 \cdot 1.5H_2O$

Typically, 4 g of V_2O_5 powder was added into 120 mL of 2 mol L^{-1} NaCl aqueous solution. The mixture was kept at 30℃ and stirred for 96 hours. The product was washed with deionized water several times till no Cl^- was detected. The final product was collected by centrifugation and dispersed in NMP to form a homogeneous slurry.

4. Fabrication of NVO Cathodes

The cathode was prepared by mixing as-prepared $NaV_3O_8 \cdot 1.5H_2O$, carbon nanotube (Macklin) and in a weight ratio of 7:2 by 1-methyl-2-pyrrolidone (NMP (>99%, Sigma-Aldrich)). After ultrasonic treatment for 60 minutes, the dispersion was collected by vacuum. Then, the NVO-CNT was mixed with PTFE (60 wt.% in H_2O, Canrd) in a ratio of 9:1 and pressed onto

stainless steel mesh (300 mesh) using a roller dried at 60℃ overnight. The mass loading of NVO was around 10 mg cm^{-2} for coin cell tests. For the pouch cell, the mass loading was further increased to around 20 mg cm^{-2}.

5. Cells Assembly

Zn||Zn symmetric, Zn||Cu, Zn||asymmetric cells, and Zn-NVO full cells were assembled in CR2025-type coin cells with the glass fiber filter (GF/D, Whatman) as the separator. The electrolyte amount used for Zn||Zn, Zn||Cu, and Zn||Ti cell configurations was 60 μL. For each coin cell with high NVO loading, 100 μL electrolyte was added.

6. Electrochemical measurement

Phase selective alternating current voltammetry (ACV) were conducted on Zn||Ti asymmetric cells under a 6 Hz frequency and 5 mV amplitude perturbation signal at a scan rate of 4 mV s^{-1} within the voltage window of 0.1 to 0.95 V versus Zn/Zn^{2+}. The capacitance (C) was calculated using the equation:

$$C = \frac{1}{2\pi f Z_{im}}$$

Electrochemical Impedance Spectroscopy (EIS) was measured on Zn||Zn and Zn-NVO cells from 100 kHz to 10 mHz with an amplitude of 6 mV to increase the signal-to-noise ratio. All data was subjected to the Kramers-Kronig validity test using “Lin-KK” tool with the relative residual was less than 1%[3]. The corresponding DRT analysis was conducted using DRT Tools[4]. For the Arrhenius equation calculation, the cells were measured at various temperature (from 30 to 70 ℃).

7. Characterizations

The chemical shifts of hydrogen atoms in various electrolytes were characterized using a 400 MHz Nuclear Magnetic Resonance Spectrometer (JEOL ECA400, Tokyo, Japan). The X-ray diffraction (XRD) patterns were obtained using a Bruker D8 Advance with Cu Kα radiation (λ=0.15418 nm). The SEM images and elemental distributions of the samples were acquired through field emission scanning electron microscopy (ZEISS SUORA®55) equipped with an energy dispersive spectrometer (EDS). The X-ray photoelectron spectra were obtained using a Shimadzu Kratos Axis Supra X-ray photoelectron spectrometer (XPS). Raman spectrometers (Horiba LabRAM HR Evolution) were used to collect Raman signals related to

solvation structures and OH^- vibrations in various aqueous electrolytes. Confocal laser scanning microscope (CLSM) images of the Zn anodes after deposition in different electrolytes were obtained using an Olympus LEXT OLS5000 laser microscope. The corresponding surface roughness was calculated based on the equation: $S_a = A^{-1}[\iint_A |Z(x,y)|dxdy]$, where S_a is the average height, S_z is the peak height, and A is the area of the measured region.

Computational Method

The Vienna Ab Initio Package (VASP)[5, 6] was employed to perform all the density functional theory (DFT) calculations within the generalized gradient approximation (GGA) using the Perdew, Burke, and Enzerhof (PBE) formulation.[7, 8] The projected augmented wave (PAW) potentials were applied to describe the ionic cores and take valence electrons into account using a plane wave basis set with a kinetic energy cutoff of 400 eV. Partial occupancies of the Kohn–Sham orbitals were allowed using the Gaussian smearing method and a width of 0.1 eV. The electronic energy was considered self-consistent when the energy change was smaller than 10^{-5} eV. A geometry optimization was considered convergent when the force change was smaller than 0.02 eV/Å. Grimme's DFT-D3 methodology was used to describe the dispersion interactions.[9-11] The equilibrium lattice constants of Zn surface were optimized when using a 3 ×3 ×1 Monkhorst-Pack k-point grid for Brillouin zone sampling. The adsorption energies (E_{ads}) are calculated as $E_{ads} = E_{molecule+slab} - E_{molecule} - E_{slab}$, where $E_{molecule+slab}$, $E_{molecule}$ and E_{slab} are the total energy of the adsorption systems, the adsorbate in the structure and the clean substrate respectively. Construction and visualization of the crystallography configurations were accomplished using VESTA software.[12]

Quantum chemistry calculations were conducted with Becke's three-parameter hybrid exchange function and Lee-Yang-Parr gradient-corrected correlation functional (B3LYP), including Grimme's DFT-D3(BJ) empirical dispersion correction. All stationary points involved were located using the 6-311G+(2d,2p) basis set. Vibrational frequency calculations at the same level were performed to ensure that these optimized geometries are true minima on the potential energy surface, evidenced by the absence of any imaginary frequencies. The binding energy (E_b) is defined as $E_b = E_{A+B} - (E_A + E_B)$, where E_{A+B} is the total energy of combined A and B and $E_A + E_B$ is the sum of the energies of single A and B molecules. A and B refer to Zn^{2+} and H_2O / furan / thiophene / pyrrole / pyridazine / Pyrazine / Pyrimidine, respectively. Visualization and data processing were conducted using Multiwfn and VMD softwares.[13, 14]

The molecular dynamics simulations (MD) were conducted through GROMACS with AMBER force field.[15, 16]The SPC/E water model was adopted, and the MD parameters for SO_4^{2-} and organic molecule were generated through Sobtop and the corresponding atom charges were based on RESP charges.[14, 17] The initial size of box was 6.3×6.3×6.3nm^3, and periodic boundary conditions were set in XYZ directions. The simulation cells contained 8300 H_2O,300 $ZnSO_4$, and 1 Pyrimidine/ Pyridazine/ Pyrazine. The electrostatic interactions were computed using PME methods. A cutoff length of 1.2 nm was used in the calculation of electrostatic interactions in real space. In both the isothermal-isochoric (NVT) and the isothermal-isobaric (NPT) ensembles, a leapfrog integrator with a time step of 1 fs was used. Temperature and pressure coupling was performed with the V-rescale and C-rescale method, respectively. These systems were minimized by the steepest descent method to limit the maximum force within 500.0kJ/(mol·nm), followed by equilibration in NVT ensemble for 1 ns at 298 K. Subsequently, a simulation of 1 ns in NPT ensemble at 1 bar was performed to reach the equilibrium. Finally, a 10 ns production simulation was carried out for post-processing analysis.

Supplementary Figures and Discussion

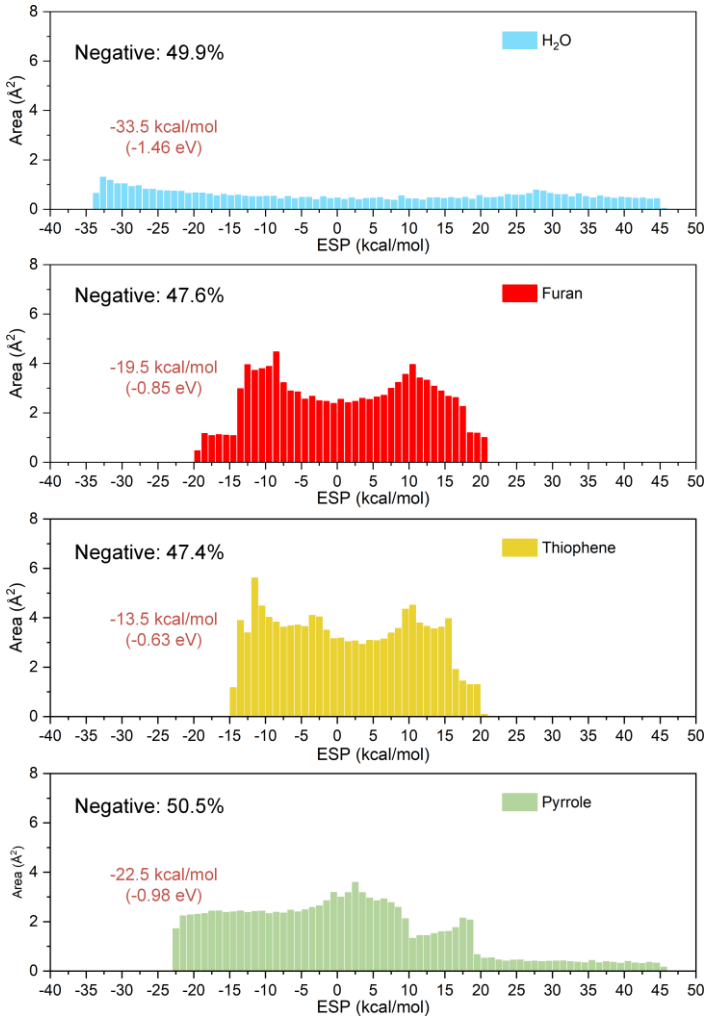

Figure S1 Distribution of ESP values for H_2O, Furan, Thiophene and Pyrrole molecules (marked negatively charged surface area ratio).

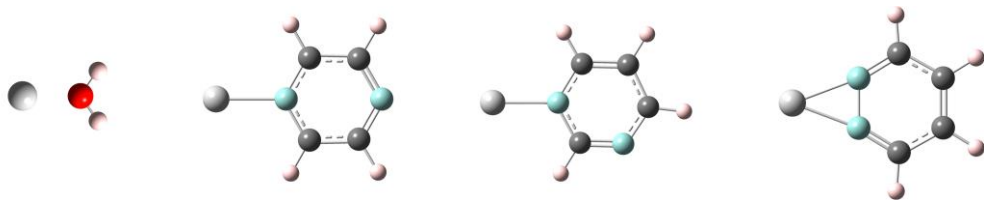

Figure S2 Adsorption configurations for various molecules and Zn^{2+} (White: Zn^{2+}, Red: O, Pink: H, Grey: C, Cyan: N).

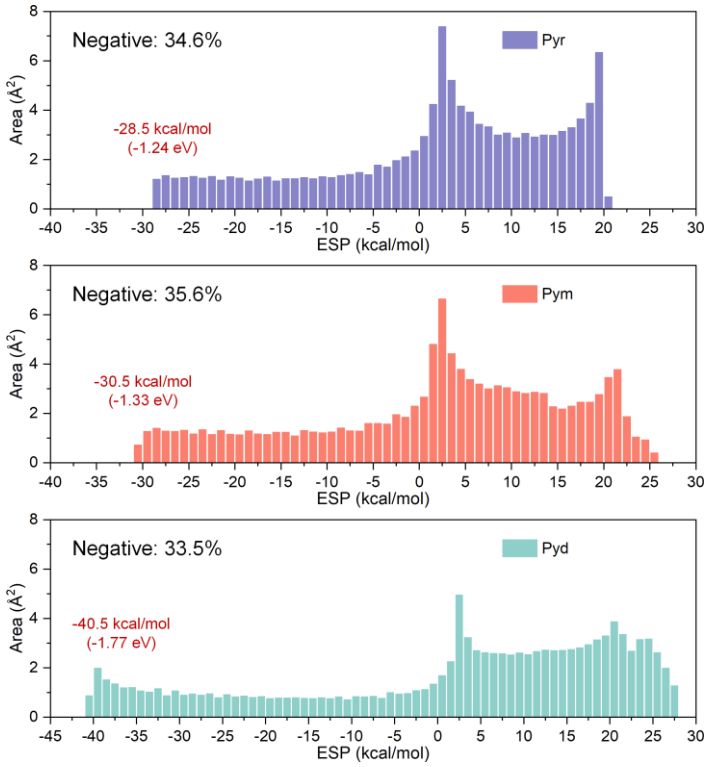

Figure S3 Distribution of surface areas for different ESP values in three molecules.

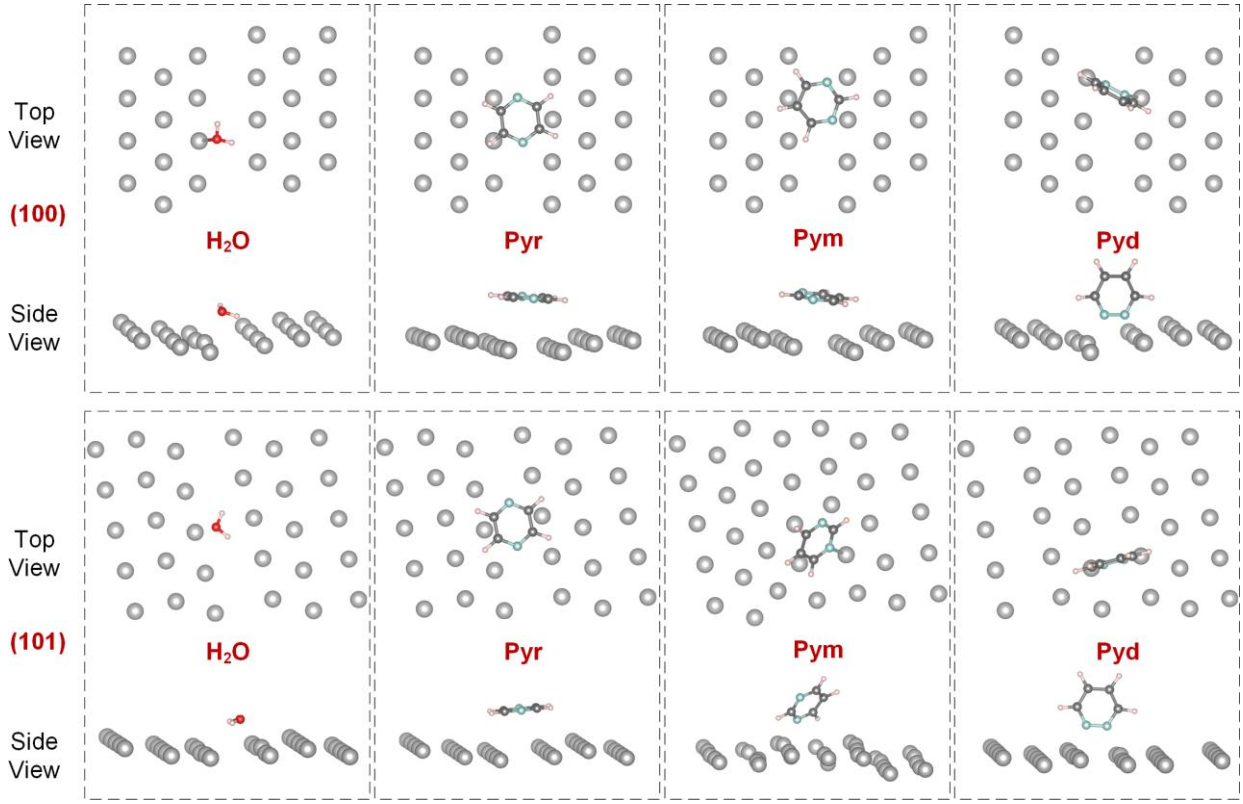

Figure S4 Optimum adsorption configurations for H_2O, Pyr, Pym and Pyd on (100) and (101) facets.

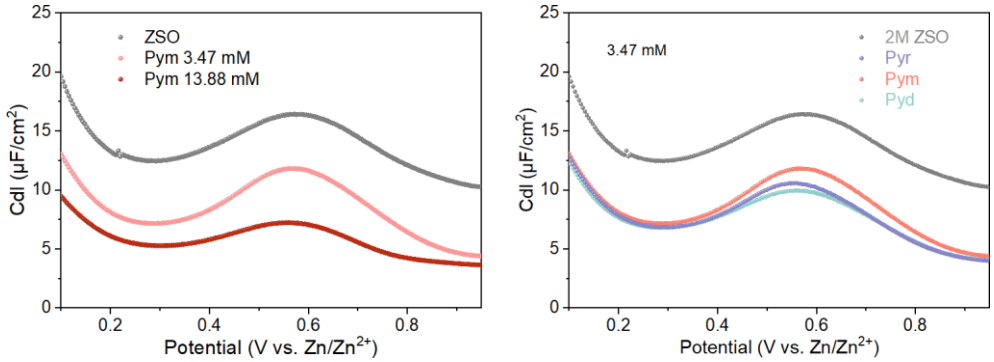

Figure S5 Differential capacitance-potential curves of Zn||Ti cells measured by ACV.

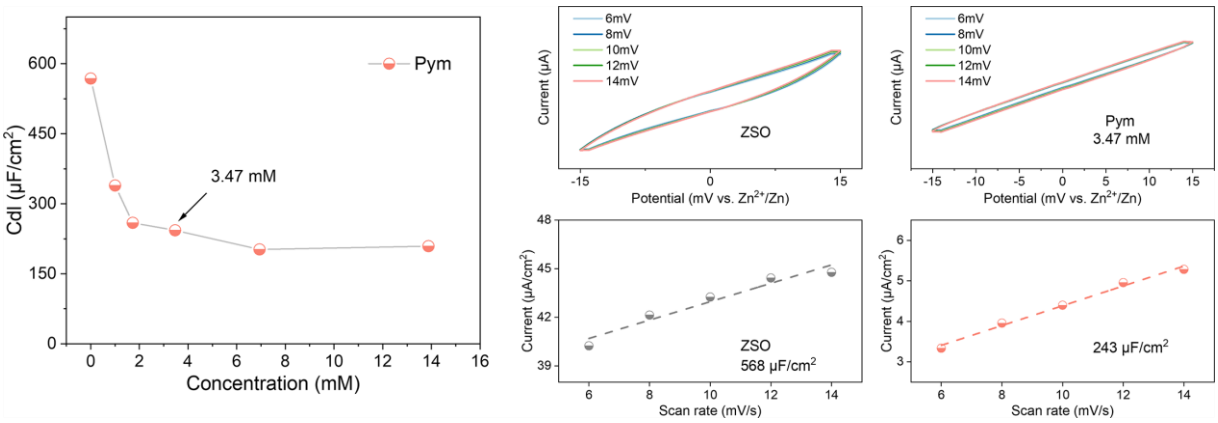

Figure S6 Electric double layer capacitance of Zn||Zn cells measured within −15 to 15 mV.

The decrease in the double-layer capacitance indicates the higher thickness of the electric double layer at Zn electrode surface due to the larger steric hindrance molecules of Pyr, Pym and Pyd adsorption. Increasing the concentration of those molecules in 2 M ZSO electrolyte further decreases the capacitance. However, the excessive adsorption of those molecules may restrict the reaction kinetics. In combination with the discussion of desired η_g and η_n, the selected concentration was 3.47 mM for further investigation.

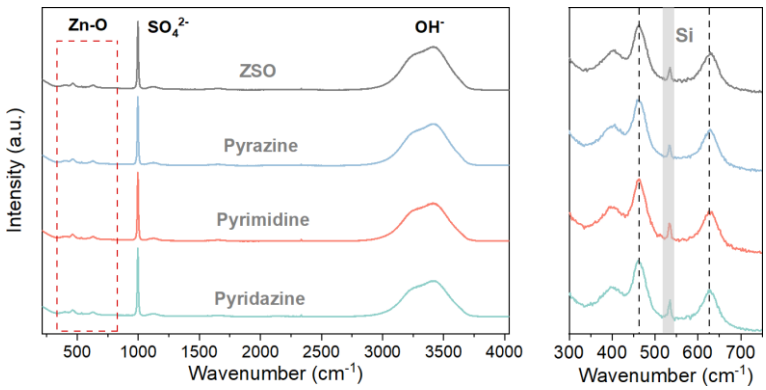

Figure S7 Raman spectra for ZSO electrolyte and ZSO with Pyr, Pym and Pyd.

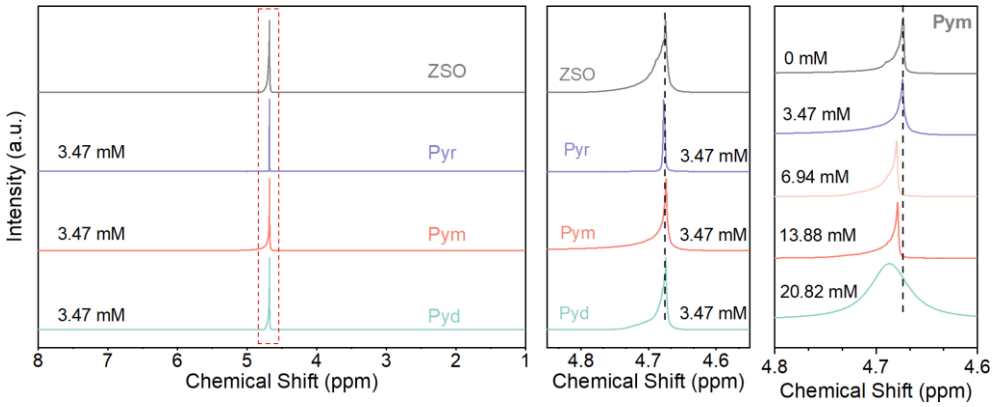

Figure S8 ^{1}H NMR Spectroscopy of ZSO and ZSO with Pyr, Pym, and Pyd electrolytes.

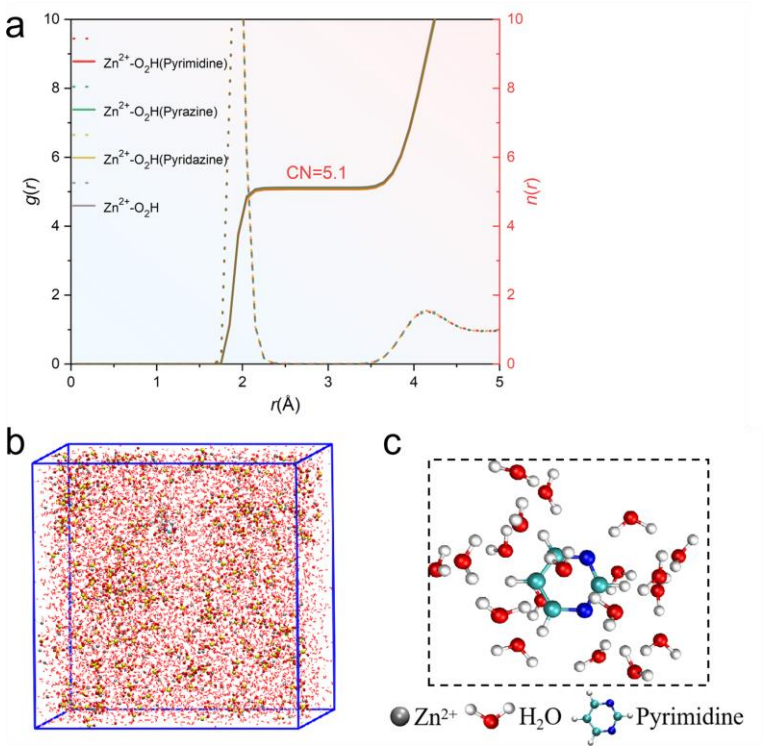

Figure S9 Molecular dynamics simulations. (a) Radial distribution functions and coordination number functions for Zn^{2+}-O_2H in different electrolytes, (b) three-dimensional snapshot for the $ZnSO_4$−Pym model and (c) the coordination environment of Pym molecule.

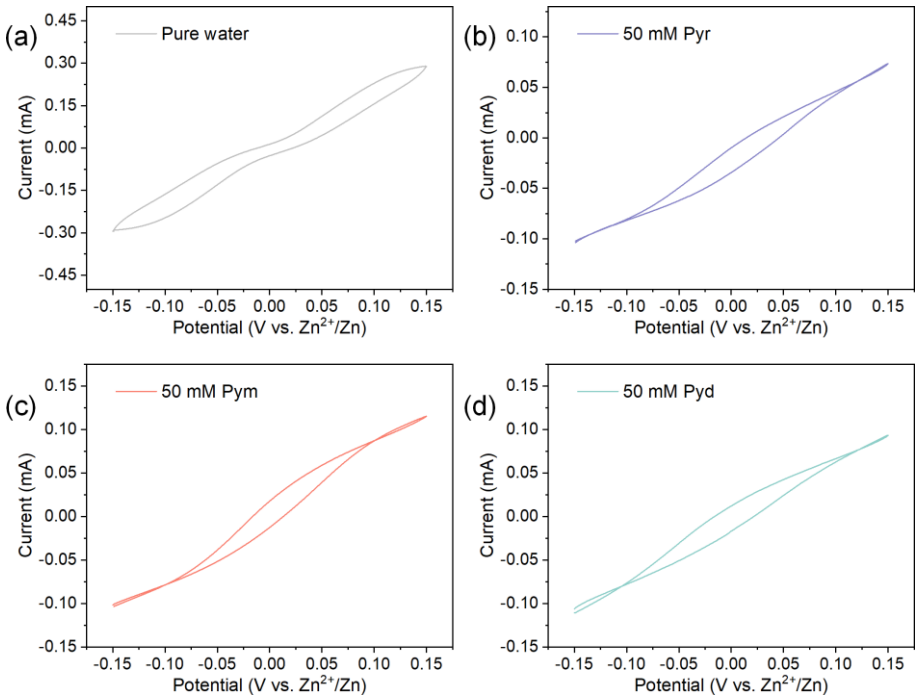

Figure S10 CV curve of Zn||Zn symmetric cell without/with 50 mM (4 g L^{-1}) Pyr, Pym, and Pyd in aqueous solution at a scan rate of 1 mV s^{-1}.

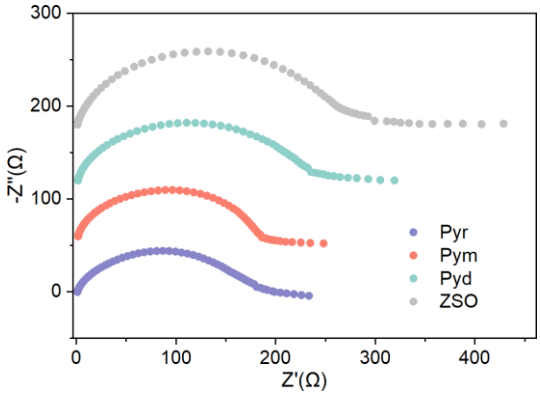

Figure S11 EIS Nyquist plots for Zn||Zn symmetric cells assembled in various electrolytes.

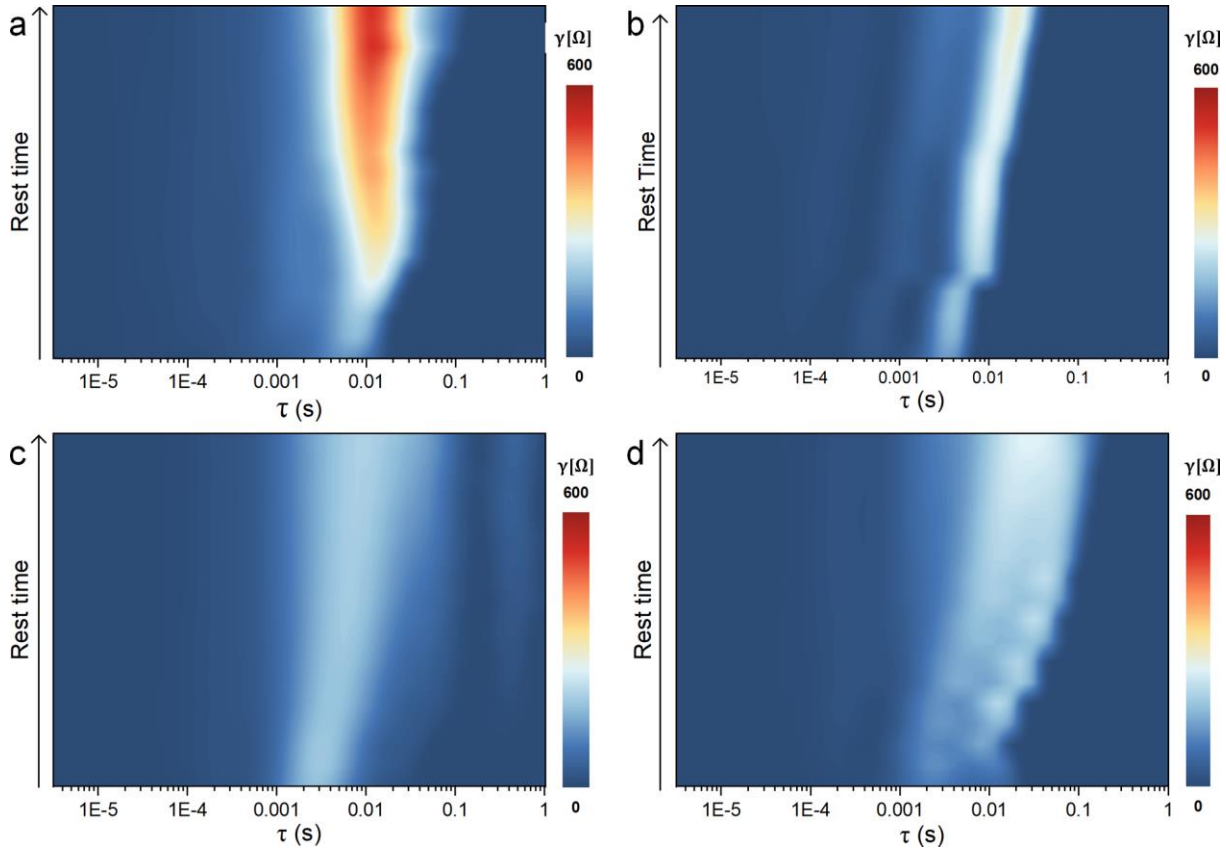

Figure S12 DRT plots for Zn||Zn cells with (a) ZSO, (b) Pyr, (c) Pym, and (d) electrolytes from freshly assembled to 12 h.

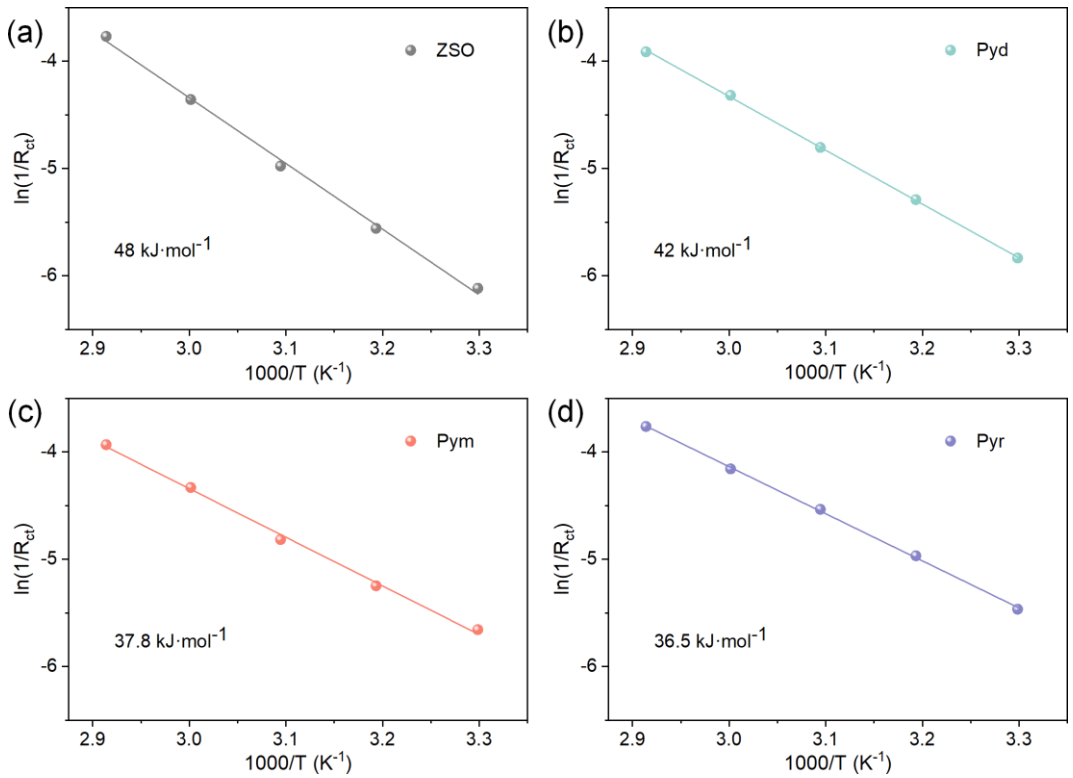

Figure S13 EIS results measured and fitted at 30 - 70 ℃ range and calculated E_a.

The activation energy (E_a) was calculated using the Arrhenius Equation:

$$\frac{1}{R_{ct}} = Aexp\left(-\frac{E_a}{RT}\right)$$

where Rct is the charge transfer resistance fitted from the semi-circle of the EIS Nyquist plots, A is the pre-exponential factor, E_a is the activation energy for the desolvation process of hydrated Zn^{2+}, R is the gas constant, and T is the temperature.

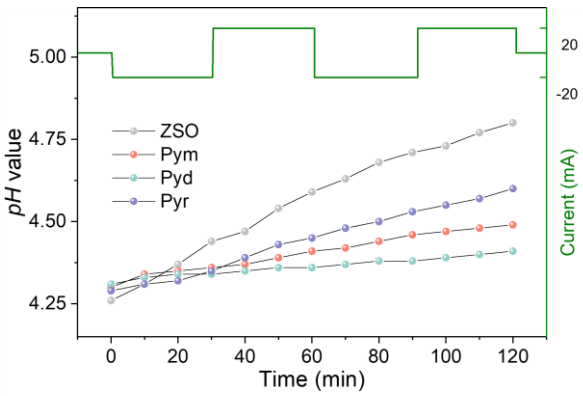

Figure S14 *In situ* monitoring of pH values in various electrolyte.

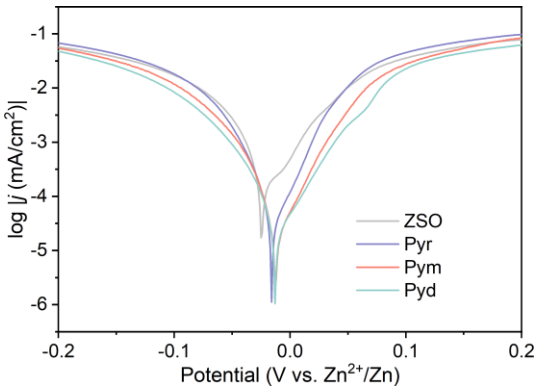

Figure S15 Tafel plots of symmetric cells measured in the voltage range of -0.2 to 0. 2 V.

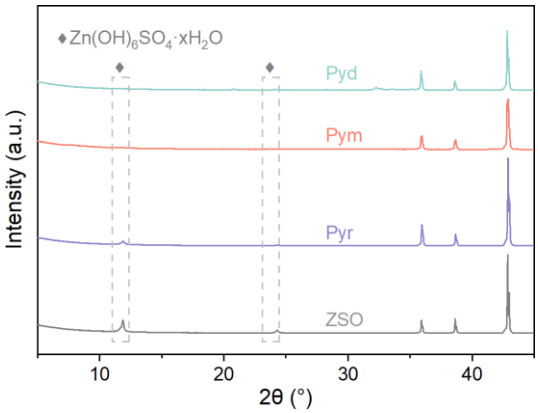

Figure S16 XRD patterns of Zn foils soaked in various electrolytes for 3 days. The marked region is diffraction peak signals for ZHS by-products[18].

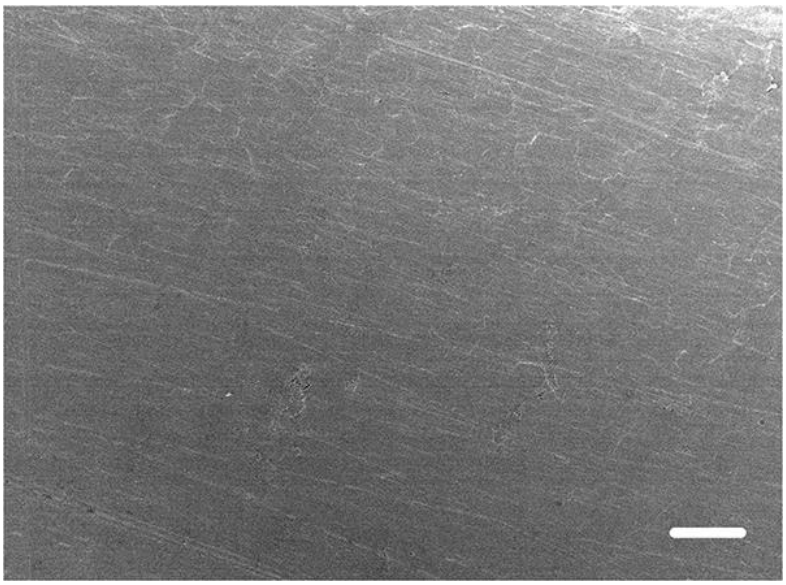

Figure S17 SEM image of fresh Zn foil (scale bar: 10 μm).

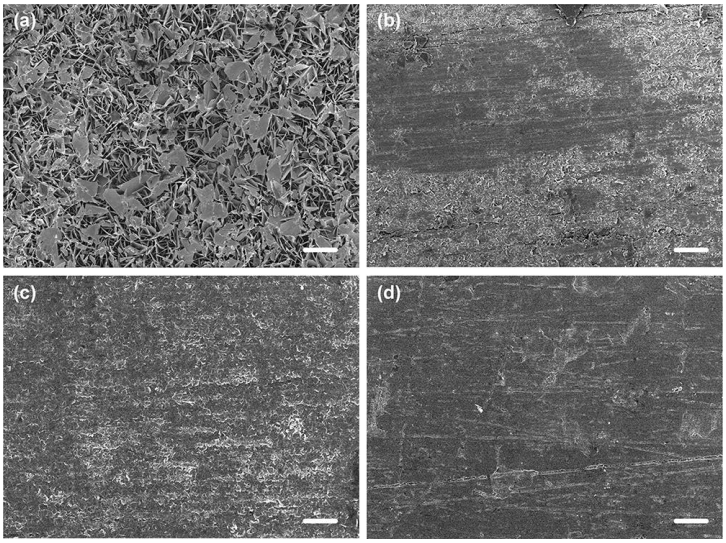

Figure S18 SEM images of Zn foils after immersing in (a) ZSO, (b) Pyr, (c) Pym, and (d) Pyd for 3 days (scale bar: 10 μm).

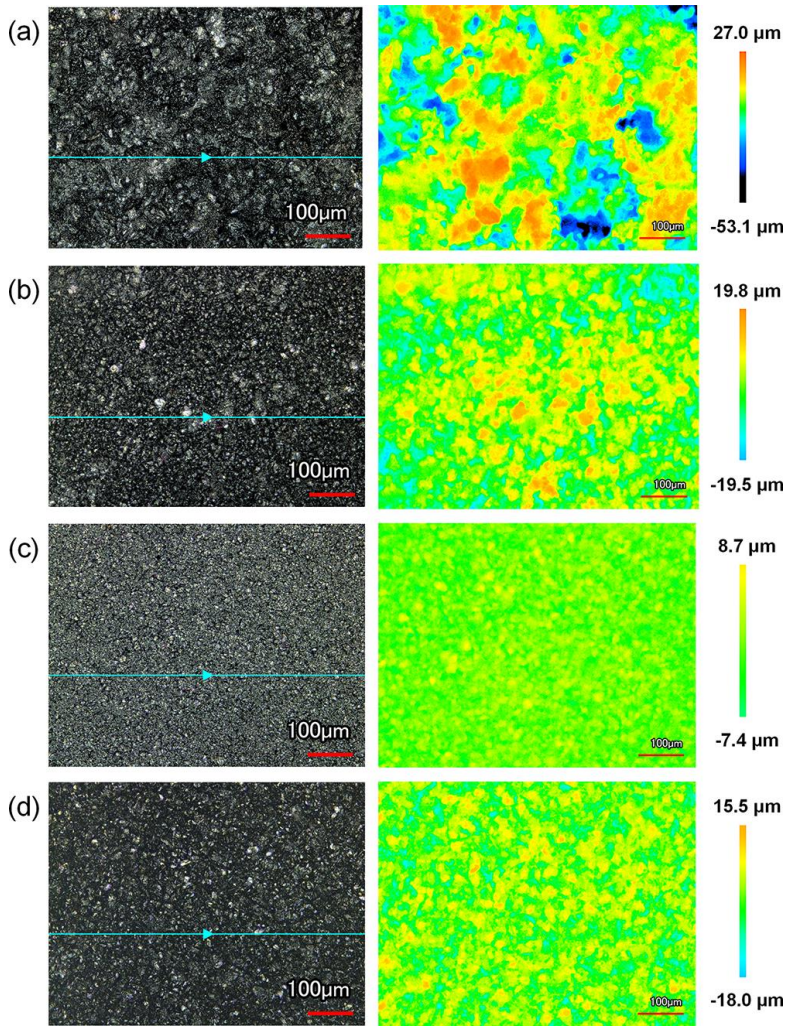

Figure S19 Optical images and corresponding 2D CLSM images of Zn deposits in (a) ZSO, (b) Pyr, (c) Pym, and (d) Pyd.

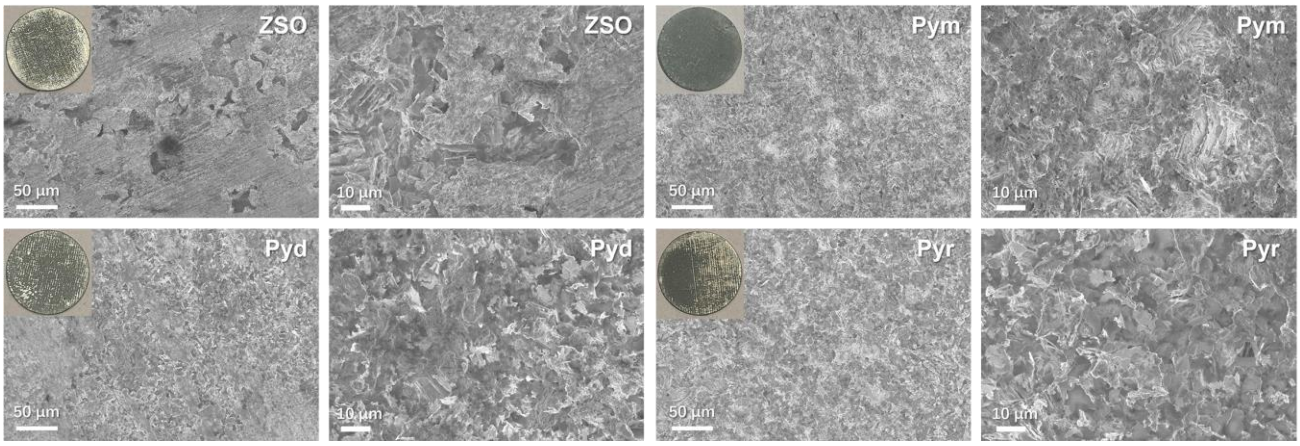

Figure S20 SEM and optical (inserted) images of Zn electrodes after stripping at 2 mA cm^{-2} for 10 mAh cm^{-2} in different electrolytes.

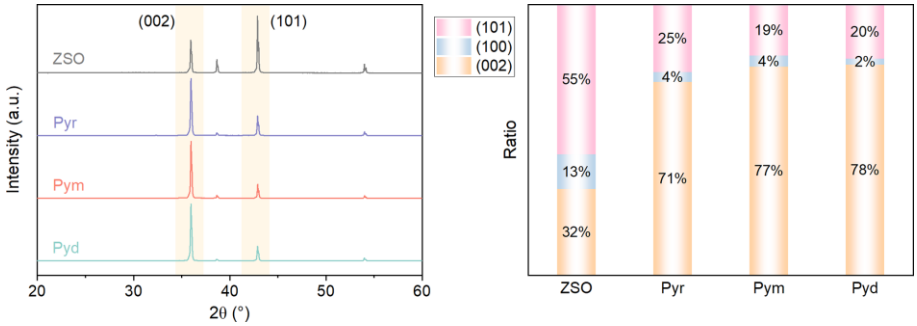

Figure S21 XRD patterns of Zn deposit in various electrolytes and intensities ratio between (002), (100), and (101) facets.

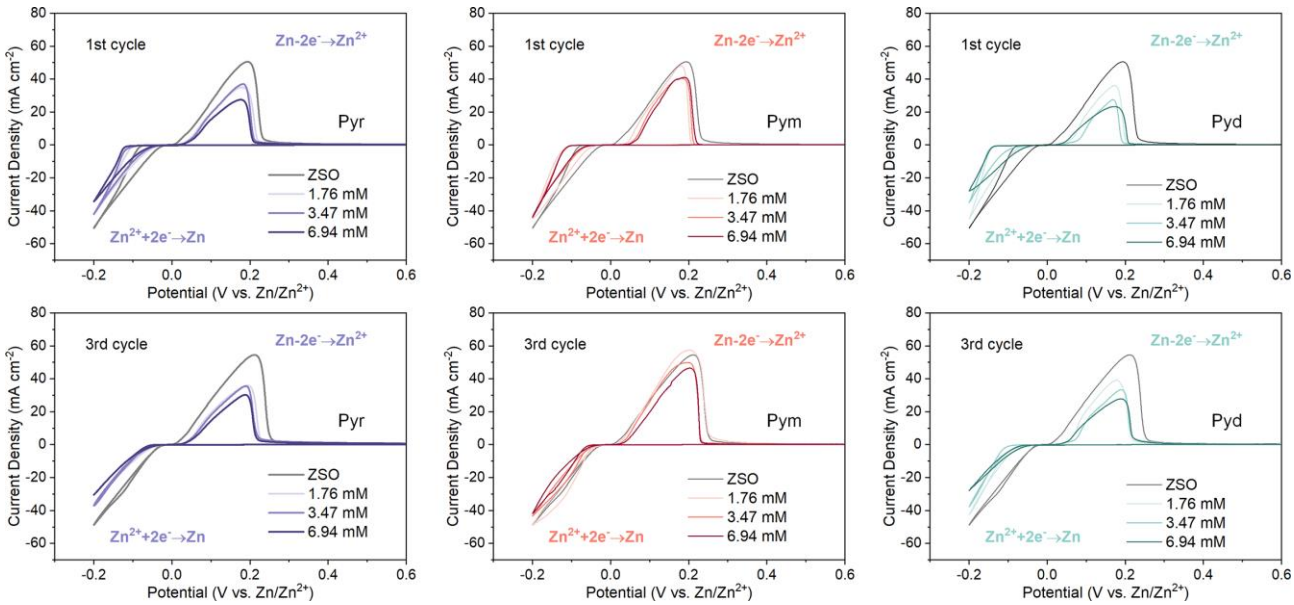

Figure S22 CV curves of Zn||Ti asymmetric cells in various electrolytes and various concentrations.

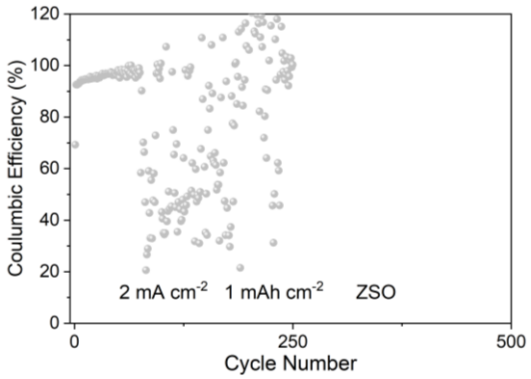

Figure S23 CE for Zn||Cu cell in ZSO electrolyte.

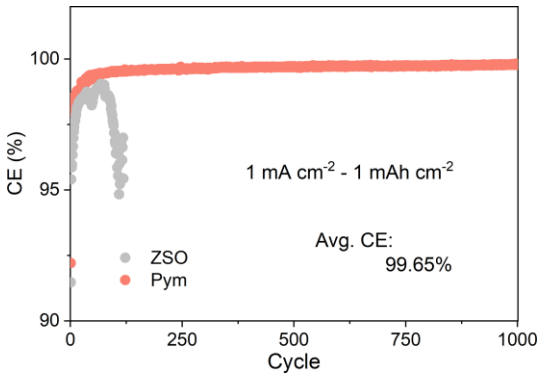

Figure S24 CE for Zn||Cu cell in ZSO and Pym electrolytes at 1 mA cm^{-2} for 1 mAh cm^{-2}.

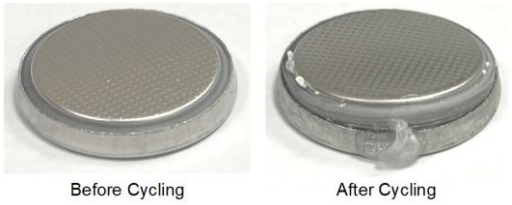

Figure S25 Optical images for the coin cell with Pyr electrolyte before and after cycling.

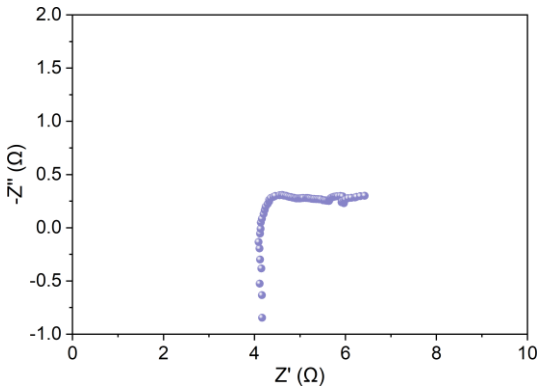

Figure S26 EIS Plot of Zn||Zn symmetric cell in Pyd after cycling.

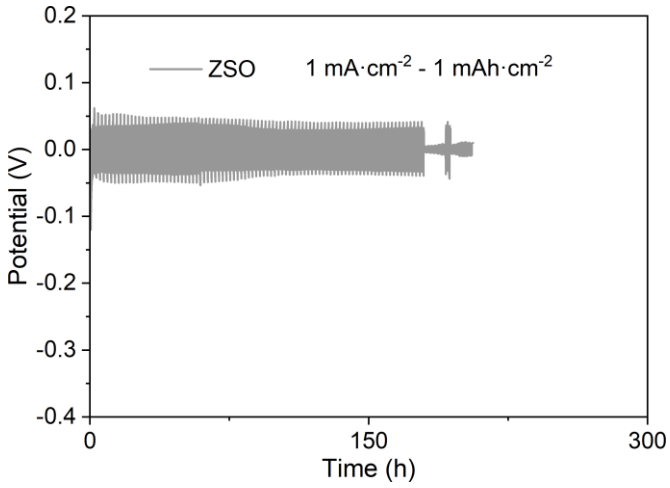

Figure S27 Cycling performance of Zn||Zn symmetric cells.

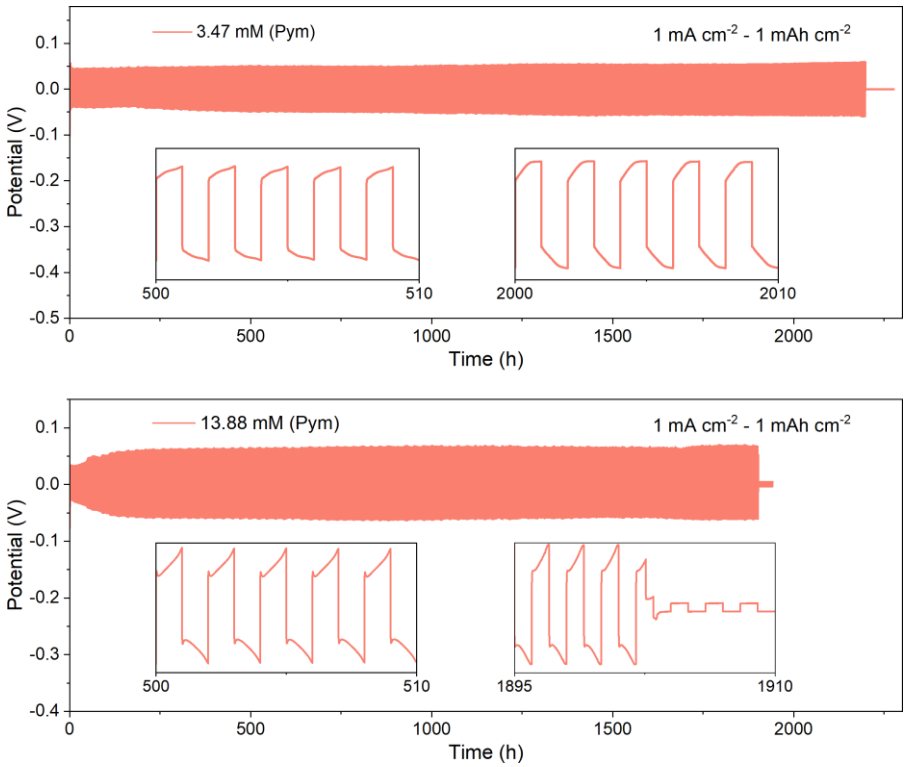

Figure S28 Long-term cycling of the Zn||Zn cell with different concentration of Pym.

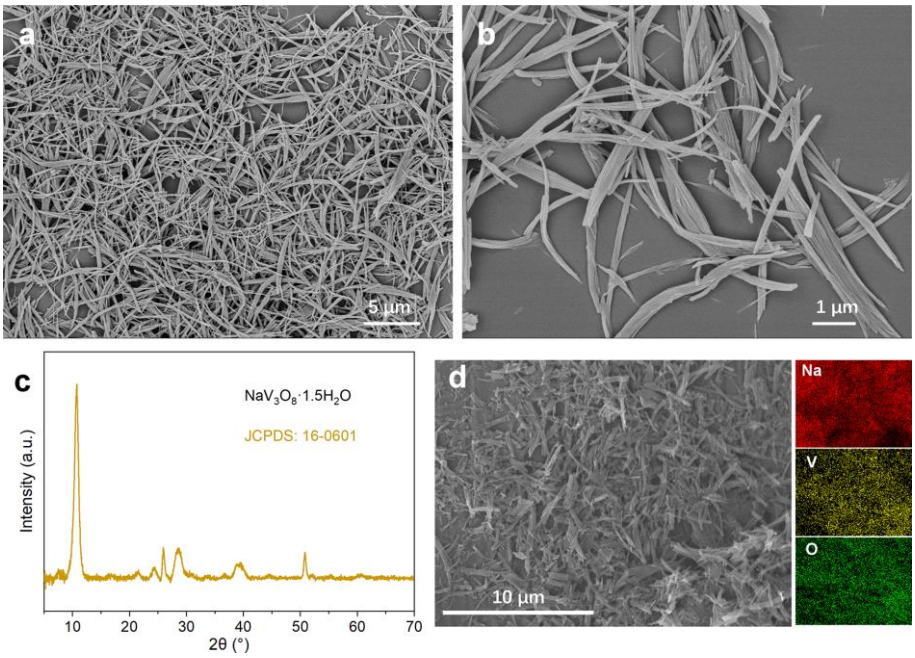

Figure S29 Morphological and structural analysis of the NVO cathode. (a-b) SEM images, (c) XRD pattern, and (d) EDS analysis.

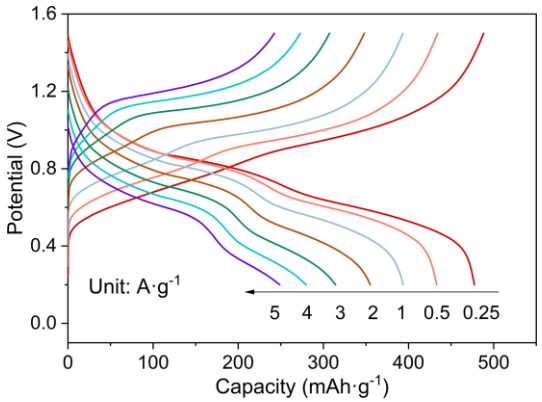

Figure S30 Galvanostatic Charge-Discharge (GCD) curves at different current densities for coin cells using Pym electrolyte.

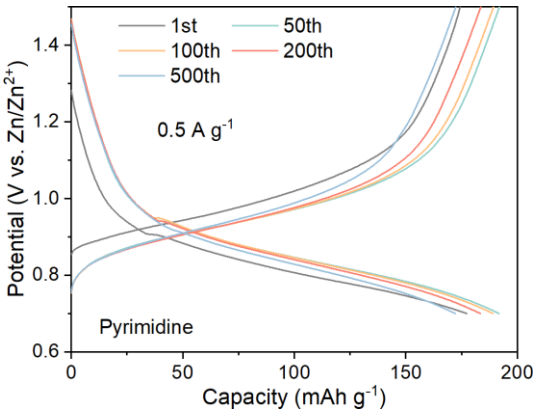

Figure S31 GCD curves at 0.5 A g^{-1} for the cell with Pym electrolyte at 1.5 - 0.6 V.

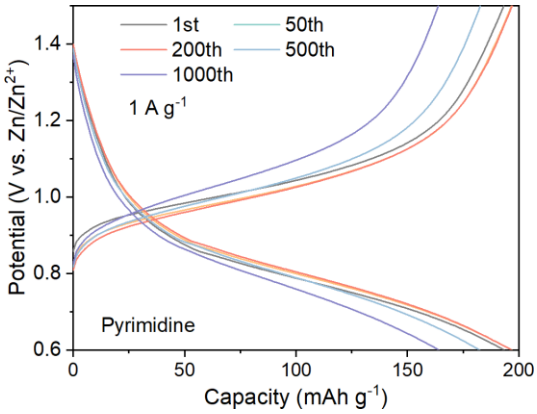

Figure S32 GCD curves at 1 A g^{-1} for coin cell using Pym electrolyte at 1.5 – 0.6 V.

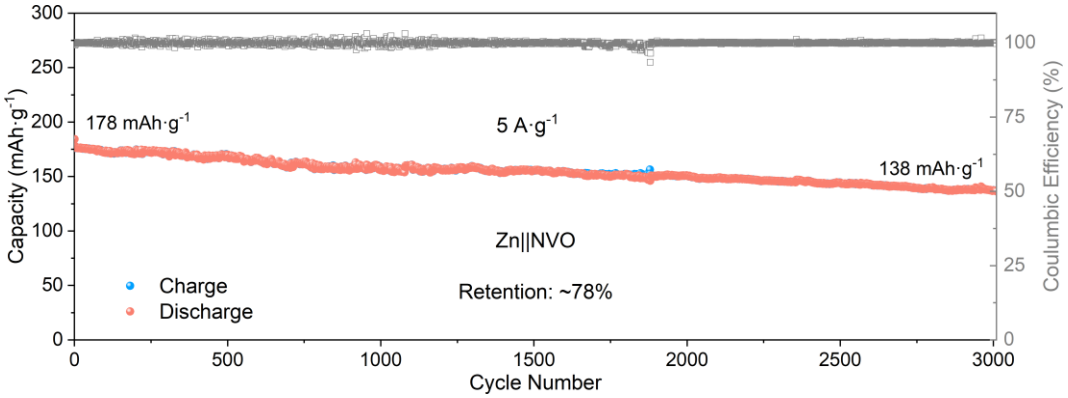

Figure S33 Cycling performance of the Zn||NVO cell at 5 A g^{-1}.

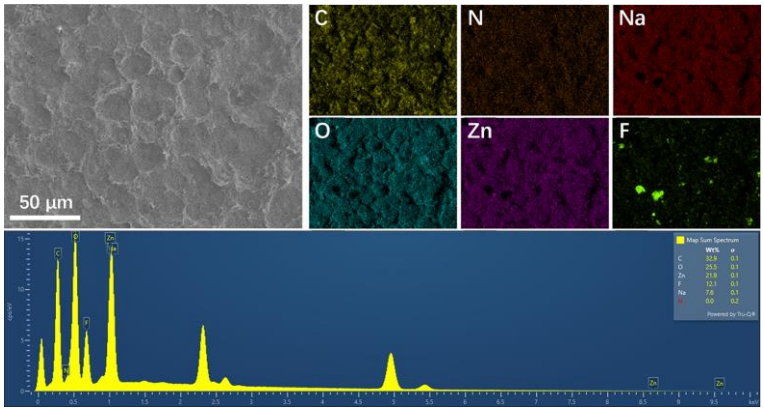

Figure S34 SEM and corresponding EDS the NVO cathode in ZSO.

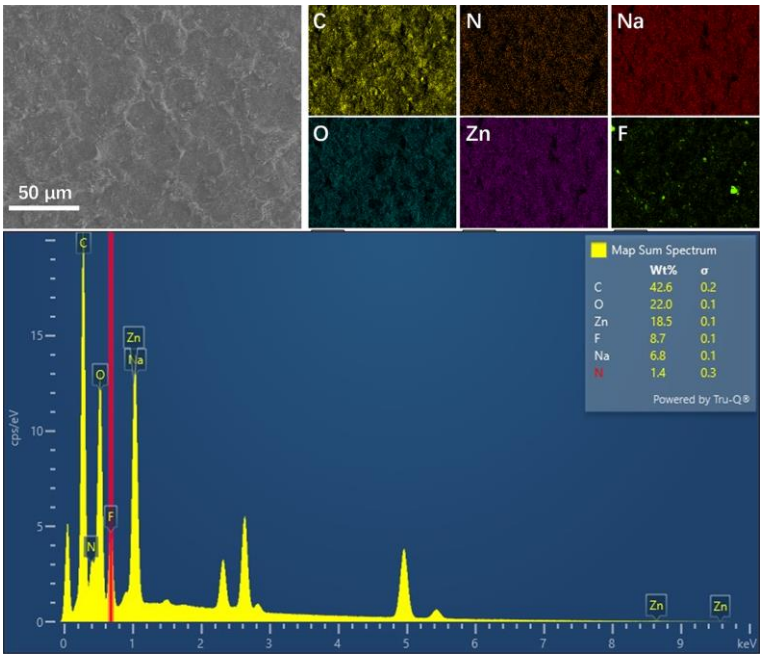

Figure S35 SEM and corresponding EDS the NVO cathode in Pym.

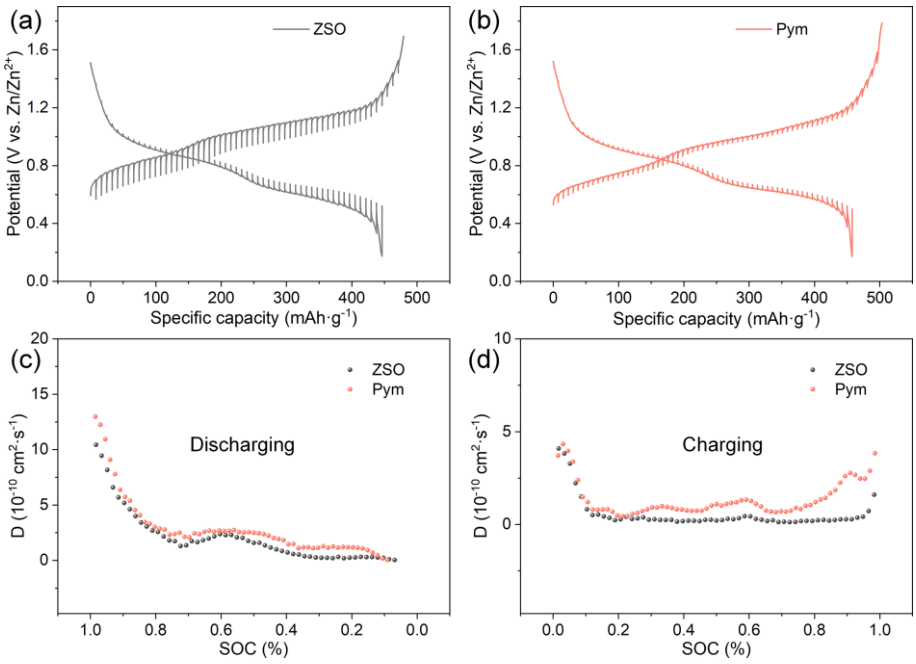

Figure S36 Voltage profiles of GITT tests for (a) ZSO and (b) Pym electrolyte, and calculated Zn^{2+} diffusion coefficients.

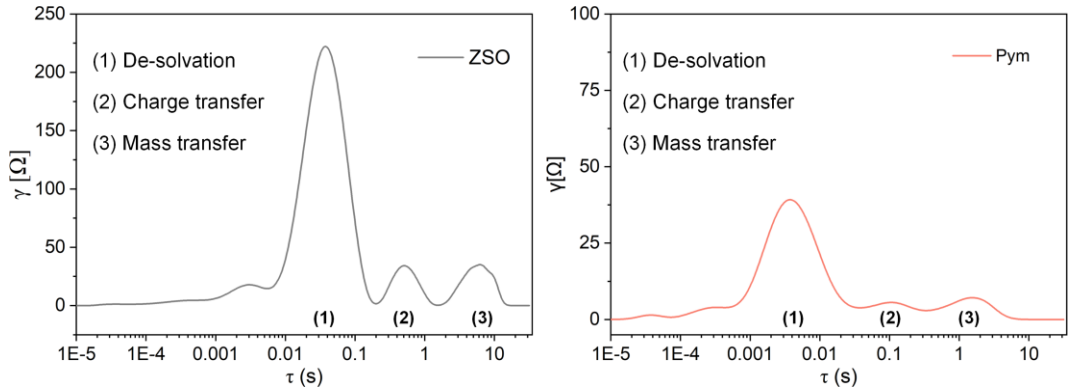

Figure S37 DRT curves of Zn||NVO full cells in ZSO and Pym discharged at 0.8V.

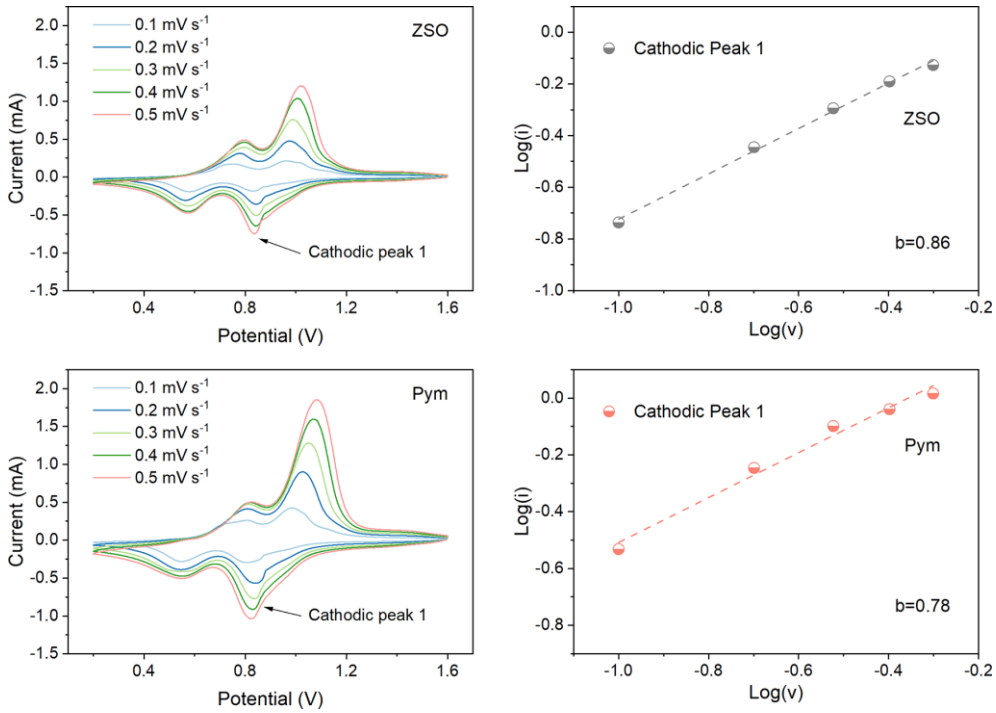

Figure S38 CV curves for Zn||NVO batteries in different electrolyte at the scan rate of 0.1 - 0.5 mV s^{-1} and corresponding linear fitting curves for the cathodic peak at around 0.8 V.

To identify the ion storage behavior in Zn||NVO batteries, we performed the CV test at different scan rates from 0.1 to 0.5 mV s^{-1}. The peak current I and the scan rate should follow the relationship: $i = av^b$, which can be rewritten as: $\log(i) = blog(v) + \log(a)$.
For b=0.5, it refers to the diffusion-controlled behavior, while for b=1 refers to the capacitive behavior.[19, 20] As shown in Figure S38, the b was 0.86 for ZSO and 0.78 for Pym, indicating the electrochemical behaviors were controlled by both ion diffusion and capacitive. Therefore, the accelerated desolvation kinetics endowed by Pym in this study is beneficial to the reaction kinetics of Zn||NVO batteries.

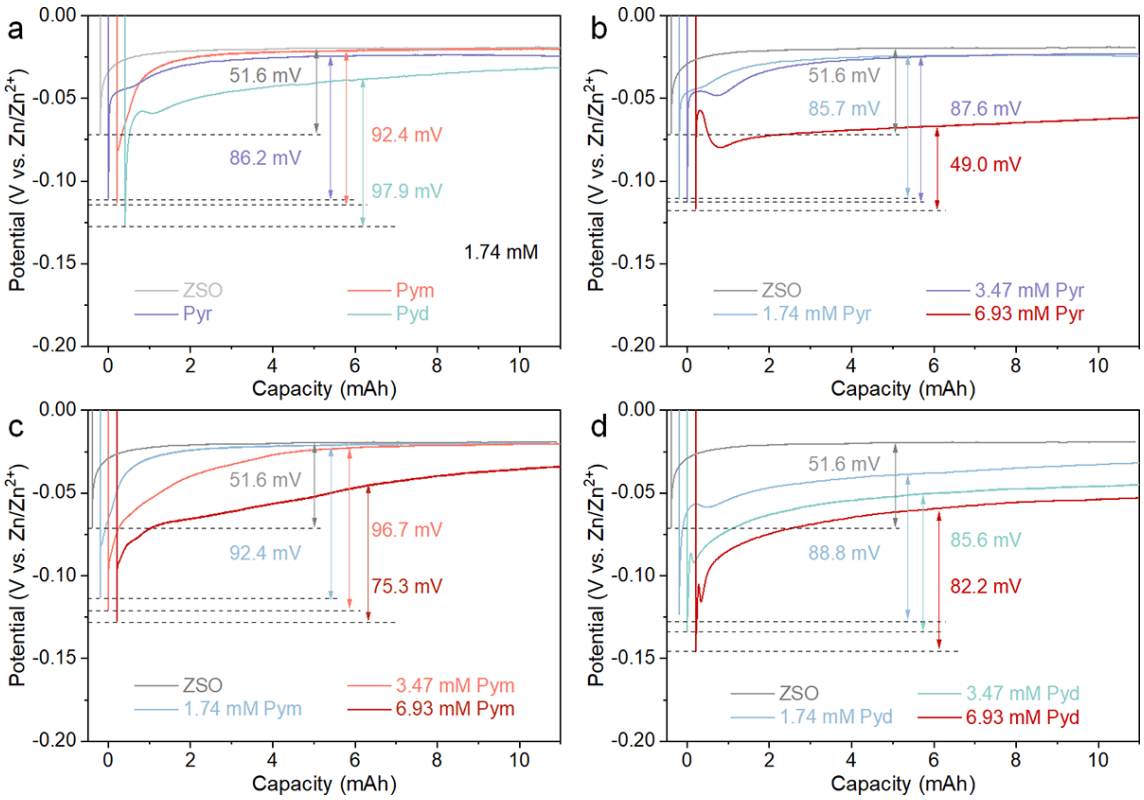

Figure S39 GCD curves of Zn||Cu cells at 5 mA cm^{-2} for 10 mAh cm^{-2}. (a) with 1.74 mM, and (b) Pyr, (c) Pym, (d) Pyd at various concentrations.

Table S1 Comparison of the Zn||Zn symmetric cell performance with recent literature.

Additives	Current (mA/cm^2)	Capacity (mAh/cm^2)	Lifespan (h)	Accumulated (mAh)	Amount	Ref.
Hexamethylenetetramine	5	1	4,000	4,000	5 mM	[21]
Butyrolactam	1	0.5	3,900	1,950	5 wt.%	[22]
Trimethyl phosphate	1	0.25	5,000	1,250	0.5 wt.%	[23]
Tetraphenyl porphyrin tetrasulfonic acid	1	1	2,300	2,300	6 mM	[24]
Pyridine	0.5	0.5	3,300	1,650	0.12 M	[25]
2,3,4,5-tetrahydroxyvaleraldehyde	2	1	950	950	0.1 M	[26]
Pym	1	1	3,000	3,000	6.94 mM	This work

Reference

1. A. Pei, G. Zheng, F. Shi, Y. Li and Y. Cui, *Nano Lett.*, 2017, **17**, 1132-1139.
2. X. Yu, Z. Li, X. Wu, H. Zhang, Q. Zhao, H. Liang, H. Wang, D. Chao, F. Wang, Y. Qiao, H. Zhou and S.-G. Sun, *Joule*, 2023, **7**, 1145-1175.
3. M. Schönleber, D. Klotz and E. Ivers-Tiffée, *Electrochim. Acta*, 2014, **131**, 20-27.
4. T. H. Wan, M. Saccoccio, C. Chen and F. Ciucci, *Electrochim. Acta*, 2015, **184**, 483-499.
5. G. Kresse and J. Furthmüller, *Computational Materials Science*, 1996, **6**, 15-50.
6. G. Kresse and J. Furthmüller, *Physical Review B*, 1996, **54**, 11169-11186.
7. J. P. Perdew, K. Burke and M. Ernzerhof, *Phys. Rev. Lett.*, 1996, **77**, 3865-3868.
8. J. P. Perdew, M. Ernzerhof and K. Burke, *The Journal of Chemical Physics*, 1996, **105**, 9982-9985.
9. S. Grimme, *J. Comput. Chem.*, 2006, **27**, 1787-1799.
10. G. Kresse and J. Hafner, *Physical Review B*, 1993, **47**, 558-561.
11. S. Grimme, S. Ehrlich and L. Goerigk, *J. Comput. Chem.*, 2011, **32**, 1456-1465.
12. K. Momma and F. Izumi, *J. Appl. Crystallogr.*, 2011, **44**, 1272-1276.
13. W. Humphrey, A. Dalke and K. Schulten, *J. Mol. Graphics*, 1996, **14**, 33-38.
14. T. Lu and F. Chen, *J. Comput. Chem.*, 2012, **33**, 580-592.
15. H. J. C. Berendsen, D. van der Spoel and R. van Drunen, *Comput. Phys. Commun.*, 1995, **91**, 43-56.
16. Y. Duan, C. Wu, S. Chowdhury, M. C. Lee, G. Xiong, W. Zhang, R. Yang, P. Cieplak, R. Luo, T. Lee, J. Caldwell, J. Wang and P. Kollman, *J. Comput. Chem.*, 2003, **24**, 1999-2012.
17. H. J. C. Berendsen, J. R. Grigera and T. P. Straatsma, *The Journal of Physical Chemistry*, 1987, **91**, 6269-6271.
18. T. Stanimirova, R. Nikolova and N. Petrova, *Crystals*, 2024, **14**, 183.
19. D. Chao, C. Zhu, P. Yang, X. Xia, J. Liu, J. Wang, X. Fan, S. V. Savilov, J. Lin, H. J. Fan and Z. X. Shen, *Nat. Commun.*, 2016, **7**, 12122.
20. F. Wan, L. Zhang, X. Dai, X. Wang, Z. Niu and J. Chen, *Nat. Commun.*, 2018, **9**, 1656.
21. H. Yu, D. Chen, Q. Li, C. Yan, Z. Jiang, L. Zhou, W. Wei, J. Ma, X. Ji, Y. Chen and L. Chen, *Adv. Energy Mater.*, 2023, **13**, 2300550.
22. Q. Guo, G. Teri, W. Mo, J. Huang, F. Liu, M. Ye and D. Fu, *Energy Environ. Sci.*, 2024, **17**, 2888-2896.

23. X. Luo, M. Zhou, Z. Luo, T. Shi, L. Li, X. Xie, Y. Sun, X. Cao, M. Long, S. Liang and G. Fang, *Energy Storage Mater.*, 2023, **57**, 628-638.
24. X. Zhao, Y. Wang, C. Huang, Y. Gao, M. Huang, Y. Ding, X. Wang, Z. Si, D. Zhou and F. Kang, *Angew. Chem. Int. Ed.*, 2023, **62**, e202312193.
25. J. Luo, L. Xu, Y. Zhou, T. Yan, Y. Shao, D. Yang, L. Zhang, Z. Xia, T. Wang and L. Zhang, *Angew. Chem.*, 2023, **135**, e202302302.
26. Y. Yang, Y. Li, Q. Zhu and B. Xu, *Adv. Funct. Mater.*, 2024, **34**, 2316371.